

## **Spatial-temporal V-Net for automatic segmentation and quantification of right ventricles in gated myocardial perfusion SPECT images**

Chen Zhao, MS<sup>1</sup>, Shi Shi, MD<sup>2</sup>, Zhuo He, BS<sup>1</sup>, Cheng Wang MD, PhD<sup>2</sup>, Zhongqiang Zhao, BS<sup>2</sup>, Xinli Li, MD, PhD<sup>2</sup>, Yanli Zhou, MD, PhD<sup>2\*</sup>, Weihua Zhou, PhD<sup>1,3\*</sup>

1. Department of Applied Computing, Michigan Technological University, Houghton, MI, 49931, USA

2. Department of Cardiology, The First Affiliated Hospital of Nanjing Medical University, Nanjing, China

3. Center for Biocomputing and Digital Health, Institute of Computing and Cybersystems, and Health Research Institute, Michigan Technological University, Houghton, MI, 49931, USA

\*Corresponding Authors:

Weihua Zhou, PhD                      E-Mail: [whzhou@mtu.edu](mailto:whzhou@mtu.edu)

Department of Applied Computing, Michigan Technological University

1400 Townsend Dr, Houghton, MI, 49931, USA

Or

Zhou Yanli, MD, PhD                      E-mail: [zhyl88@qq.com](mailto:zhyl88@qq.com)

Department of Cardiology, The First Affiliated Hospital of Nanjing Medical University,

300 Guangzhou Rd, Gulou, Nanjing, 210000, China;

## **Abstract**

**Background.** Functional assessment of right ventricles (RV) using gated myocardial perfusion single-photon emission computed tomography (MPS) heavily relies on the precise extraction of right ventricular contours. In this paper, we present a new deep learning model integrating both the spatial and temporal features in SPECT images to perform the segmentation of RV epicardium and endocardium.

**Methods.** By integrating the spatial features from each cardiac frame of gated MPS and the temporal features from the sequential cardiac frames of the gated MPS, we develop a Spatial-Temporal V-Net (S-T-V-Net) for automatic extraction of RV endocardial and epicardial contours. In the S-T-V-Net, a V-Net is employed to hierarchically extract spatial features, and convolutional long-term short-term memory (ConvLSTM) units are added to the skip-connection pathway to extract the temporal features. The input of the S-T-V-Net is an ECG-gated sequence of the SPECT images and the output is the probability map of the endocardial or epicardial masks. A Dice similarity coefficient (DSC) loss which penalizes the discrepancy between the model prediction and the ground truth is adopted to optimize the segmentation model.

**Results.** Our segmentation model was trained and validated on a retrospective dataset with 34 subjects, and the cardiac cycle of each subject was divided into 8 gates. The proposed ST-V-Net achieved a DSC of 0.7924 and 0.8227 for the RV endocardium and epicardium, respectively. The mean absolute error, the mean squared error, and the Pearson correlation coefficient of the RV ejection fraction between the ground truth and the model prediction are 0.0907, 0.0130 and 0.8411.

**Conclusion.** The results demonstrate that the proposed ST-V-Net is an effective model for RV segmentation. It has great promise for clinical use in RV functional assessment.

**Keywords:** Myocardial perfusion SPECT, right ventricle, deep learning, image segmentation

## 1. Introduction

Currently, myocardial perfusion single-photon emission computed tomography (MPS) is mainly used to detect myocardial perfusion defect and evaluate cardiac function of left ventricles. Studies have quantitatively evaluated right-ventricular (RV) function in MPS and demonstrated their diagnostic and prognostic values[1-3]. Nevertheless, RV functional assessment is often ignored during the MPS examination due to the challenges in identifying RV and extracting its contours in these images. It is important to develop algorithms and techniques for RV segmentation and subsequent functional assessment in MPS.

Most of the automated myocardial segmentation methods using MPS are based on traditional image processing and the segmentation targets are left ventricles (LV). The commercial method presented by Germano et al counted the profiles for myocardial walls and employed the Gaussian filter to smoothen the boundaries [4]. Huang et al. [5] presented a region-based active contour model to perform the LV myocardium segmentation according to the scalable fitting energy and local image fitting energy. The designed model achieved a Dice score of 0.7946 for LV segmentation using short-axis gated MPS. Sonesson et al. [6] employed the Dijkstra's algorithm to find an optimal mid-mural line within myocardial wall and then to search for the epicardial and endocardial contours based on the signal intensity and the myocardial wall thickness. However, without image feature extraction and feature selection, the LV myocardium would be over- or under-segmented using traditional image processing-based methods.

In recent years, machine learning and deep learning-based methods were integrated into automatic myocardium segmentation. Betancur et al. [7] employed a support vector machine with hand-crafted image features to perform the mitral valve plane localization, which is the prepositive step for LV myocardium segmentation and MPI quantification. Wang et al. [8] proposed a multi-channel 3D V-Net for LV segmentation in MPS. Using physician-confirmed LV contours as the learning-based labels, the 3D multi-class V-Net architecture enabled voxel-wise error back-propagation during the training stage, directly outputting an equal-sized prediction patch with the input patch during the testing procedure and achieved a Dice score of 0.926 for left myocardium segmentation. Due to its data-driven and automatic feature extraction, this deep learning-based method significantly outperformed the traditional image processing methods and machine learning approaches. However, the V-Net can only extract spatial features, and the temporal features from the contextual cardiac frames in gated MPS are ignored, though they are important for sequential MPS image feature extraction.

Manual segmentation of the right ventricle (RV) is time consuming, tedious and subjective; thus the automated methods are desired in clinical practice. However, automatic identification of RV is challenging due to the ambiguous boundary, irregular cavity and the shape changes considerably. Evaluation of RV function is more difficult than LV because of RV anatomy [9]. The RV is pyramidal in shape, with an inlet, a main body, and an outflow tract; thus, the borders are difficult to outline [10]. In addition, RV wall thickness typically is a third of that of the LV, exacerbating

difficulties of RV segmentation. The RV in general has low counts on MPS. All these factors make it much more difficult to evaluate RV anatomy and function than it is to evaluate the same for LV in MPS. Nevertheless, the RV is visible on MPS in certain patient populations including dilated cardiomyopathy and pulmonary hypertension. In our study [11], RV dyssynchrony was measured by phase analysis of gated FDG-PET in patients with pulmonary hypertension and validated with the contraction delay measured by speckle tracking echocardiography; furthermore, it showed significant correlation with RV dysfunction. In our other study [12], both LV and RV dyssynchrony was measured from gated SPECT MPI and the difference between them was used to define the interventricular mechanical dyssynchrony; there was an excellent agreement between the interventricular mechanical dyssynchrony and bundle branch block patterns identified by ECG. Both studies employed a template-based method to sample RV myocardial wall for functional assessment, which is a major technical limitation [10]. As a result, it is important to develop a more accurate and robust segmentation method for improved RV functional assessment.

To the best of our knowledge, this paper presents the first study for RV segmentation using MPS and a deep learning method. In this paper, a deep learning-based method is presented for RV epicardium and endocardium segmentation. In detail, a Spatial Temporal V-Net (S-T-V-Net) is presented to extract both spatial and temporal features from 4D MPS imaging sequence. The input of the S-T-V-Net is a sequence of the MPS images containing the cropped volumes from 2 to 8 gates, and the output of the S-T-V-Net is the probability map of the endocardial or epicardial masks for the volume from the last gate in the input sequence. A Dice similarity coefficient loss, which penalizes the discrepancy between the model predicted RV masks and the ground truths, is adopted to optimize the model. The proposed S-T-V-Net achieved a Dice of 0.8303 and 0.8290, and an average surface distance of 0.3942 and 0.3508 pixels for RV epicardium and endocardium segmentation, respectively.

## **2. Materials and Methods**

### **2.1. Study Population**

This retrospective study enrolled 34 subjects who received MPS scans from May 2012 to September 2016. Coronary artery disease, myocardial infarction, dilated cardiomyopathy, and hypertrophic cardiomyopathy in dilation stage were included. The average age was  $57 \pm 12$  years, 68% were men, and congestive heart failure in twelve patients (29%). Thirty patients (73%) had abnormal perfusion on MPS. All subjects underwent standard 12-lead ECG-gated MPS. All subjects were enrolled from the First Affiliated Hospital of Nanjing Medical University. The study was approved by the Institutional Ethical Committee of the First Affiliated Hospital of Nanjing Medical University, and the written informed consent forms were obtained from all participants.

### **2.2 Myocardial $^{99m}\text{Tc}$ -sestamibi Scintigraphy**

The gated rest MPS was performed around 60 minutes post injection using 20-30 mCi of Tc- $^{99m}$  sestamibi. SPECT planar images were acquired with a dual-headed camera (Philips Medical Systems, Milpitas, CA, USA) using a standard resting protocol. The imaging parameters were 20% energy window around 140KeV, 180o orbit, and 32 steps with 25 seconds per step, 8-bin gating, and 64 projections per gate. The total acquisition time was 14 minutes

for each patient. Image reconstruction and reorientation were completed with Emory Reconstruction Toolbox (ERToolbox; Atlanta, GA). SPECT images were reconstructed by ordered subset expectation maximization (OSEM) with 3 iterations and 10 subsets and then filtered by a Butterworth low-pass filter with a cut off frequency of 0.4 cycles/cm and an order of 10.

The voxel spacing in each scanned gate in MPS is fixed at 6.4 mm. A well-trained cardiologist manually annotated the contours for both epicardial and endocardial myocardium for each gate of the MPS.

### 2.3. S-T-V-Net

We formulate RV segmentation as a spatiotemporal sequence segmentation problem in which the input is spatiotemporal sequence and the prediction target is a 3D volume where 1 represents the epicardium or endocardium, and 0 indicates the background. Suppose that the gated MPS is denoted as  $\mathcal{X}_i \in R^{H \times W \times D}$ , where  $i$  is the index of the gate (cardiac frame) in a gated MPS sequence, and  $H$ ,  $W$  and  $D$  indicate the height, width and depth of the MPS volume at gate  $i$ . The RV segmentation problem is further converted into predicting the contours of epicardium or endocardium for MPS at gate  $t$ , as shown in Eq. 1.

$$\mathcal{Y}_{i+t} = \underset{\mathcal{X}_i, \dots, \mathcal{X}_{i+t}}{\operatorname{argmax}} p(\mathcal{Y}_{i+t} | \mathcal{X}_i, \mathcal{X}_{i+1}, \dots, \mathcal{X}_{i+t}) \quad (1)$$

where  $\mathcal{Y}_i$  is the mask of epicardium or endocardium of the MPS volume  $\mathcal{X}_i$ .

The proposed SPECT RV myocardium segmentation model, which is called S-T-V-Net, contains a V-Net and convolutional long-term short-term memory (LSTM) units. The architecture of the proposed S-T-V-net is shown in Figure 1.

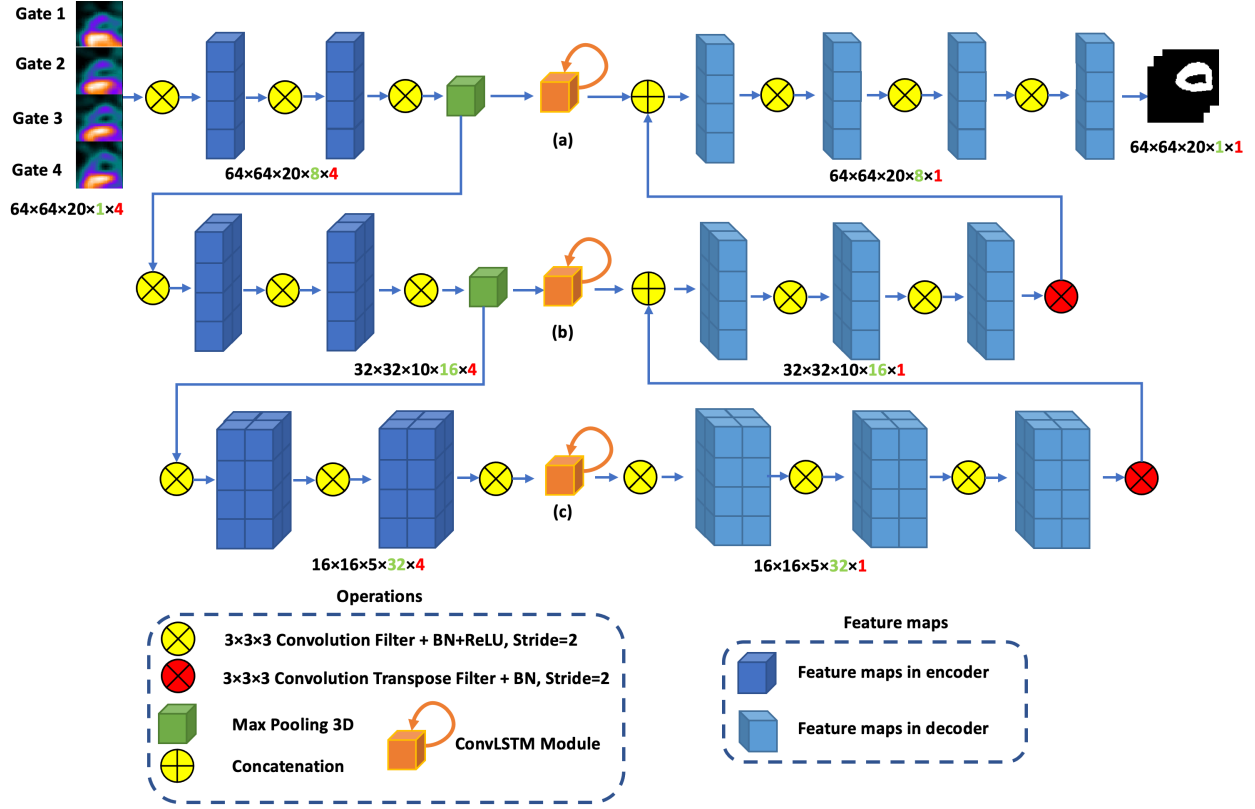


**Figure 1.** Architecture of the proposed S-T-V-Net for RV segmentation. This figure presents an example using 4 gated MPS volumes as the input and the output is the probability map for segmentation of the 4-th gated MPS. The corresponding numbers in black, green and red indicate the dimension of the feature maps, the number of the feature map and the length of the temporal sequence.

#### (1) V-Net for spatial feature extraction.

V-Net was proposed by [13], which has been widely used for three-dimensional medical image segmentation. The presented V-Net contains an encoder and a decoder. The encoder contains 6 convolutional layers and 2 max-pooling layers to jointly extract hierarchical features from spatial aspect, which enhances the feature representation ability of the convolutional neural network (CNN) [14]. The decoder contains 10 convolutional layers to restore the down-sampled features and generate the final predictions. The skip connections from the down-sampling path to the up-sampling path are adopted to recover spatially detailed information by reusing feature maps. A concatenation operator is adopted to fuse features from the encoder and decoder. In each CNN layer, a batch normalization layer [14] and an ReLU activation layer are employed to prevent the model from overfitting and accelerate model training.

#### (2) Convolutional LSTM (ConvLSTM) for sequence modeling.

Fully connected LSTM has shown powerful performance for handling temporal correlations [15]. It contains an input gate, a forget gate and an output gate. The major innovation of LSTM is its memory gate which gradually accumulates the state information along with the input sequence. Every time the input feature maps  $x_t$  comes, the memory cell  $c_t$

accumulates the information if the input gate  $i_t$  is activated. Meanwhile, the past memory  $c_{t-1}$  is removed if the forget gate  $f_t$  is activated. The output of the LSTM is further controlled by the output gate  $o_t$  and the current memory cell  $c_t$ .

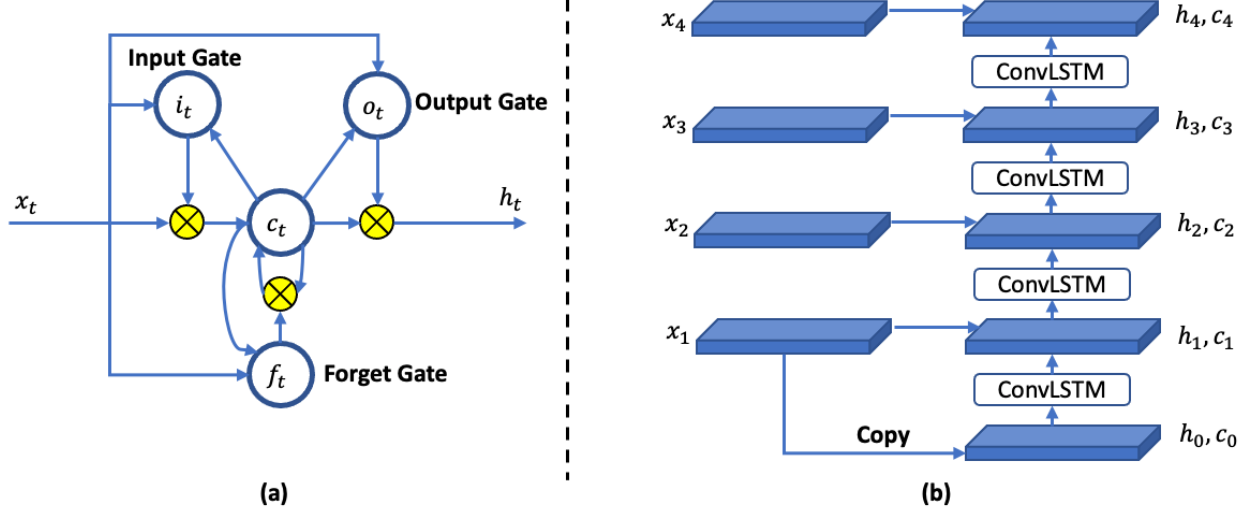


**Figure 2.** (a) Architecture of the ConvLSTM unit. (b) Dataflow of ConvLSTM for processing a sequential data with 4 cardiac frames of MPS.

However, the major deficiency of fully connected LSTM in handling spatiotemporal data is its requirement for converting feature maps into feature vectors so that the spatial information will be lost. By replacing the fully connected layers in the LSTM unit with the convolutional operations in input gate, forget gate, and output gate, the ConvLSTM was proposed [16]. The detail architecture of a LSTM cell is shown in Figure 2 (a) and the equation of ConvLSTM is shown in Eq. 2.

$$\begin{aligned}
 i_t &= \sigma(W_i * x_t + U_i * h_{t-1} + V_i \circ c_{t-1}) \\
 f_t &= \sigma(W_f * x_t + U_f * h_{t-1} + V_f \circ c_{t-1}) \\
 c_t &= f_t \circ c_{t-1} + i_t \circ \sigma(W_c * x_t + U_c * h_{t-1}) \\
 o_t &= \sigma(W_o * x_t + U_o * h_{t-1} + V_o \circ c_t) \\
 h_t &= o_t \circ \sigma(c_t)
 \end{aligned} \tag{2}$$

where  $*$  represents convolutional operator in Figure 2 (a) and  $\circ$  represents Hadamard product. The  $W$ ,  $U$  and  $V$  indicate the convolutional kernels in corresponding gates.  $x_t$  is the input of the ConvLSTM module, and  $h_t$  is the hidden output.

By stacking multiple ConvLSTM layers, we build a network to encode both spatial and temporal features of the MPS sequence. The initial memory cell is copied from the input feature maps and the memory cell is updated according to the input sequential MPS. In detail, the initial hidden state and the memory cell are copied from the feature maps  $x_1$  extracted by V-Net from the first MPS  $\mathcal{X}_1$ . Then the ConvLSTM dynamically accumulates the hidden states and the

feature maps from the memory cell to calculate the last hidden state, i.e.  $h_4$ . The inner dataflow of the ConvLSTM is shown in Figure 2 (b). In our implementation, the ConvLSTM module in Figure 1 contains two ConvLSTM layers, and each gate has 8 feature maps. By applying ConvLSTM layers to the sequential MPS, the feature maps for the last MPS are obtained. Then the feature maps are directly concatenated with the feature maps from the transpose layer in the decoder of V-Net.

### 2.3. Optimization and Evaluation

The proposed RV myocardium segmentation method consists of a training stage and a testing stage. We apply a 5-fold cross validation to train and test the model. A compound loss function that consists of a Dice similarity coefficient (DSC) loss and an L1 regularizer is employed to optimize the model weights. The DSC measures overlaying between the segmented volumes and the ground truth, as defined in Eq. 3.

$$DSC = \frac{2|Y \cap Y'|}{|Y| + |Y'|} \quad (3)$$

where  $Y$  is the ground truth of epicardium or endocardium,  $Y'$  is the predicted mask of epicardium or endocardium and  $|\cdot|$  indicates the number of foreground (epicardium or endocardium) voxels within the specific volume. To penalize the discrepancy between the generated epicardial or endocardial mask and the ground truth, and deal with the data imbalance issue [17, 18], a DSC loss is adopted to optimize the weights of the S-T-V-Net. In addition, to prevent model from overfitting, an L1 regularization is added to the loss function. The overall objective function is defined in Eq. 4.

$$Loss = -\frac{2|Y \cap Y'|}{|Y| + |Y'|} + |W|_1 \quad (3)$$

where  $W$  represents the weights of S-T-V-Net and  $|W|_1$  is the L1 regularizer.

The designed S-T-V-Net was implemented in Python using Pytorch with the backend of a CUDA version 10.2. We trained the model on a workstation with a NVIDIA TITAN V100 GPU with 32GB RAM. Each model was trained for 1000 epochs using an Adam optimizer with a learning rate of 0.001. During the model training, we adopted the random flip and the random rotation within 15 degrees to perform data augmentation.

To evaluate the model performance, we firstly check the generated contours of epicardium and endocardium visually. To quantitatively reflect the voxel difference, we adopt DSC, sensitivity (SN), and specificity (SP) to evaluate the model performance. The SN measures the proportion of the true positive (TP) voxels compared to the number of TP and false negative (FN) voxels, while the SP measures the proportion of true negative (TN) voxels compared to the number of TN and false positive (FP) voxels. The definition of SN and SP is shown in Eq. 4 and Eq. 5. A DSC, SN and SP of 1 indicates a perfect match between the model prediction and the ground truth; on the contrary, 0 represents total mismatch.

$$SN = \frac{TP}{TP + FN} \quad (4)$$



$$SP = \frac{TN}{TN + FP} \quad (5)$$

To measure the surface distance between the predicted masks and the ground truth, we employ Hausdorff distance (HD) and average surface distance (ASD) to evaluate the model. The Hausdorff distance measures the maximum distance between the predicted myocardium surface and the ground truth. The ASD indicates the average distance between the predicted myocardium surface and the ground truth.

Moreover, we calculated RV ejection fraction (EF) to further evaluate the proposed S-T-V-Net. The volume inside the endocardial surface of myocardium is defined as RV cavity. The maximum and minimum volumes inside the epicardial surface of myocardium are denoted as the end-diastolic volume (EDV) and end-systolic volume (ESV), respectively. The RVEF is then calculated as:

$$RVEF = \frac{EDV - ESV}{EDV} \quad (6)$$

We evaluated the similarity between the RVEF derived by the model segmentation results and the ground truth using mean squared error (MAE), mean absolute error (MSE) and Pearson correlation coefficient (PCC). The definition of MAE, MSE and PCC are shown in Eq. 7-9.

$$MAE = \frac{1}{N} \sum_{i=1}^N |r_e^i - r_g^i| \quad (7)$$

$$MSE = \frac{1}{N} \sum_{i=1}^N (r_e^i - r_g^i)^2 \quad (8)$$

$$PCC = \frac{\sum_{i=1}^n (r_e^i - \bar{r}_e)(r_g^i - \bar{r}_g)}{\sqrt{\sum_{i=1}^n (r_e^i - \bar{r}_e)^2} \sqrt{\sum_{i=1}^n (r_g^i - \bar{r}_g)^2}} \quad (9)$$

where  $r_e^i$  indicates the estimated RVEF using segmentation results, and  $r_g^i$  represented the ground truth of the RVEF.  $N$  is the sample size and  $i$  is the index of the training sample. And  $\bar{r}_e$  and  $\bar{r}_g$  are the mean values of the corresponding measurements.

### 3. Experimental Results

#### 3.1. Baseline Models

To reflect the effectiveness the proposed model, two baseline models were implemented by removing the ConvLSTM module and V-Net module, thus a plain V-Net and a Spatial-Temporal-Net (S-T-N) were obtained. The architectures of the baseline models are shown in Figure 3.

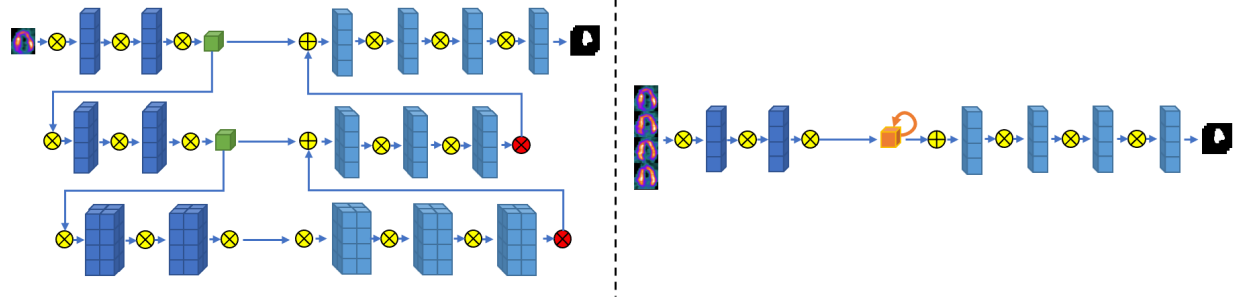


**Figure 3.** Baseline models. *Left:* V-Net, which is obtained by removing the ConvLSTM modules and its input only contains one gate of MPS. *Right:* S-T-Net, which is obtained by removing the pooling layers in V-Net.

### 3.2. Segmentation Results

Firstly, we tested the models with 4 gates of MPS as the sequential MPS, and Table 1 quantitatively compares the model performance of the baseline models and the proposed S-T-V-Net for RV epicardium and endocardium segmentation, respectively. The performance is reported according to the subjects from the test set in each cross-validation fold.

**Table 1.** Quantitative evaluation for the V-Net, S-T-Net, and S-T-V-Net for RV epicardium and endocardium segmentation. DSC, Dice similarity coefficient; HD, Hausdorff distance; ASD, average surface distance; SN, sensitivity; SP, specificity. Except V-Net, all models were trained with a sequential MPS containing volumes from continuous 4 gates. The bold text indicates the model achieved the best performance within the corresponding task.

Class	Model	DSC	HD (pixel)	ASD (pixel)	SN	SP
Epicardium	V-Net	0.7691	12.6640	0.6288	0.7851	0.9323
	S-T-Net	0.6718	18.2887	1.0397	<b>0.9906</b>	0.7006
	S-T-V-Net	<b>0.8296</b>	<b>11.8385</b>	<b>0.3704</b>	0.8421	<b>0.9465</b>
Endocardium	V-Net	0.6299	13.0329	1.0623	0.6926	0.9658
	S-T-Net	0.6163	20.8996	1.0638	<b>0.9749</b>	0.9073
	S-T-V-Net	<b>0.7964</b>	<b>9.5624</b>	<b>0.4230</b>	0.7984	<b>0.9824</b>

According to Table 1, the proposed S-T-V-Net achieved the highest DSC, SP, and lowest ASD and HD on our MPS dataset for both epicardium and endocardium segmentation. The epicardial and endocardial contours generated by different models of the representative slices are shown in Figure 4.

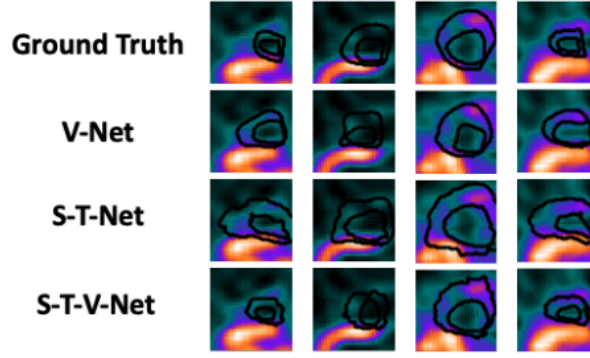


**Figure 4.** Comparison of the segmentation results from different models. (a), images with manually annotated epicardial and endocardial contours; (b), images with contours generated by V-Net; (c), images with contours generated by S-T-Net, and (d), images with contours generated by S-T-V-Net.

We further validated the proposed model using MPS sequence with different number of gates, as shown in Table 2.

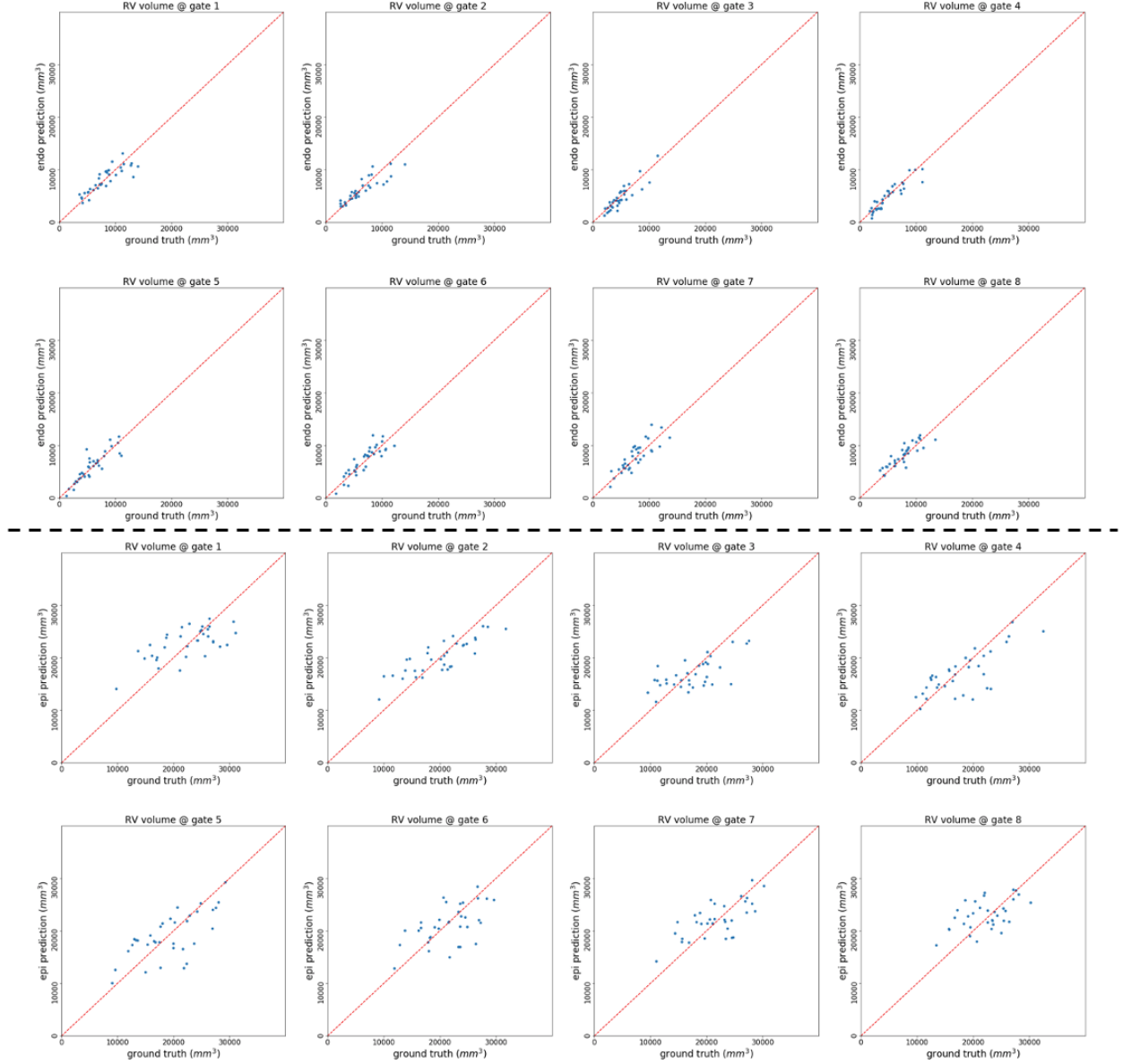
**Table 2.** Quantitative evaluation of S-T-V-Net for RV epicardium and endocardium segmentation using different gate numbers of MPS. In V-Net, only one gate was used as the input. The bold text indicates that the model achieves the best performance with the corresponding parameters.

Class	# Gates	DSC	HD (pixel)	ASD (pixel)	SN	SP
Epicardium	2	0.8127	11.1071	0.3562	0.8446	0.9474
	3	0.7964	9.5624	0.4230	0.7984	0.9824
	4	0.8296	11.8385	0.3704	0.8421	0.9465
	5	0.8016	9.4399	0.3848	0.8034	0.9851
	6	0.8290	11.8094	<b>0.3508</b>	<b>0.8494</b>	0.9426
	7	<b>0.8303</b>	<b>9.0445</b>	0.3942	0.8225	<b>0.9899</b>
	8	0.8283	11.6288	0.3844	0.8464	0.9432
Endocardium	2	0.7981	9.1848	0.3941	0.8032	0.9843
	3	0.8127	11.1071	0.3562	0.8446	0.9474
	4	0.7964	9.5624	0.4230	0.7984	0.9824
	5	0.8226	11.8385	0.3704	0.8421	0.9465
	6	0.8016	9.4399	0.3848	0.8034	<b>0.9851</b>
	7	<b>0.8290</b>	<b>8.8094</b>	<b>0.3508</b>	<b>0.8494</b>	0.9426
	8	0.8003	9.0445	0.3942	0.8225	0.9829

According to Table 2, the proposed S-T-V-Net achieved the best DSC and HD when the gate number of the MPS sequence was set as 7 for both epicardium and endocardium segmentation.

### 3.3. Results of RVEF quantification

Before evaluating the performance of RVEF prediction, we inspected the volumes of the endocardium and epicardium derived by model prediction and ground truth for each gate, as shown in Figure 5 (a) and (b).

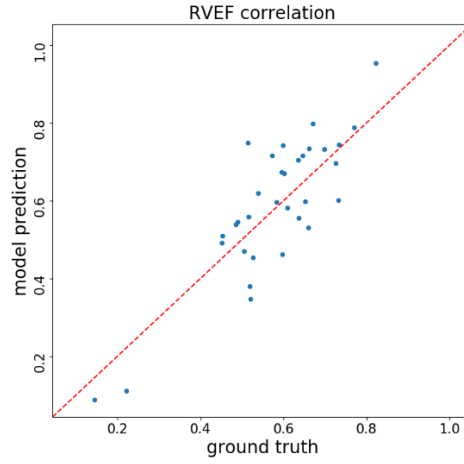


**Figure 5.** Endocardial volumes (top four) and epicardial volumes (bottom four) measured from the ground truth and our proposed method. Blue dots indicate the measurement of each subject at the corresponding gate, and the red line represents the identity line.

We calculated the RVEF using the RV endocardial volumes measured from our proposed method and compared it with the RVEF measured from the manually annotated RV endocardial contours. The results are shown in Table 3. Also, we inspected the RVEF derived by the segmentation results using S-T-V-Net and the corresponding ground truth, as shown in Figure 6.

**Table 3.** Evaluation of RVEF results by different segmentation models.

Model	# Gates	MAE	MSE	PCC
V-Net	-	0.5936	0.5106	-0.1192
S-T-Net	4	0.2400	0.0718	0.5909
S-T-V-Net	2	0.0960	0.0156	0.7810
S-T-V-Net	3	0.3172	1.7013	-0.0614
S-T-V-Net	4	0.0942	0.0152	0.8304
S-T-V-Net	5	0.0880	0.0120	0.8341
S-T-V-Net	6	0.3549	2.4504	-0.2223
S-T-V-Net	7	0.0907	0.0130	<b>0.8411</b>
S-T-V-Net	8	<b>0.0863</b>	<b>0.0112</b>	0.8394

**Figure 6.** Plot of RVEFs measured from the ground truth and our proposed method. Blue dots indicate the measurement of each subject, and the red line represents the identity line.

## 4. Discussion

### 4.1. Performance of RV segmentation

In this study, the results strongly demonstrate the feasibility of the proposed model in clinical practice for the delineation of the RV epicardial and endocardial contours. According to Table 1, the proposed S-T-V-Net achieved the best DSC and lowest ASD for epicardium and endocardium segmentation compared to those two baseline models. For epicardium segmentation, the S-T-V-Net improved the DSC from 0.7691 achieved by V-Net to 0.8296, and decreased ASD from 0.6288 pixels achieved by V-Net to 0.3704 pixels; for endocardium segmentation, the S-T-V-Net improved the DSC from 0.6299 achieved by V-Net to 0.7964, and decreased ASD from 1.0623 pixels achieved by V-Net to 0.4230 pixels. In Figure 4, the comparison of the segmentation results indicates that the epicardial and endocardial contours generated by S-T-V-Net were closer to the ground truth than those of V-Net and S-T-V-Net.

The comparison between the S-T-V-Net and V-Net indicates that adding ConvLSTM layers to V-Net was effective for capturing temporal features according to the MPS sequence, and thus the S-T-V-Net achieved a better performance.

The comparison between the S-T-V-Net and S-T-Net demonstrates that adding pooling layers to hierarchically extract spatial features was important for RV segmentation. The results show that the S-T-V-Net is effective in modeling spatiotemporal data for RV myocardium segmentation using four-dimensional imaging.

From Table 2, we can observe that with the increment of the gates in the MPS sequence, the performance of S-T-V-Net firstly increased to its peak when the gate number of the MPS was set as 7, and then slight degraded. In detail, the S-T-V-Net achieved its best DSC using the MPS sequence with 7 gates for both epicardium and endocardium segmentation. With the increment of gates, i.e. from 2 to 7, the temporal information was well captured by the proposed S-T-V-Net. This is because integrating contextual temporal features are important for video prediction [19], and the cardiac motion is traceable within a cardiac cycle. However, increasing the gates in a sequence greedily, i.e. from 7 to 8, didn't further improve the segmentation performance.

#### **4.2 Clinical values of RV segmentation and functional assessment**

According to Table 3, the proposed S-T-V-Net with 8 gates in MPS achieved the best MAE and MSE for RVEF evaluation. And with 7 gates in MPS, the S-T-V-Net achieved the highest PCC between the model prediction and the ground truth. The results further validated that the S-T-V-Net was more powerful than the V-Net and S-T-Net.

During the past decades, RV functional assessment was neglected in the diagnosis and prognosis of left-sided heart failure. However, it was clearly demonstrated that RV dysfunction not only existed in left heart failure with reduced ejection fraction (HFrEF) and with preserved ejection fraction (HFpEF), but also strongly contributed to the increase of morbidity and mortality [20, 21]. Right heart function is an indicator to measure the severity of pulmonary hypertension and pulmonary arterial hypertension (PAH) often becomes increasingly complicated due to right heart dysfunction. Moreover, improvement of right heart function is important to evaluate the therapeutic effect and prognosis of PAH. Therefore, it is essential to measure valuable parameters to assess RV function in HF and PAH patients.

Right heart catheterization (RHC) is commonly used to measure RV hemodynamic parameters and is the gold standard for PAH diagnosis. However, first, RV cardiac output (CO) is commonly measured by thermodilution in RHC, which may overestimate CO in patients with decreased cardiac function [22]. Second, as an invasive test, RHC requires hospitalization, which limits its clinical application in primary diagnosis and follow-up. Echocardiography is the most widely used right heart functional test, but it also has many disadvantages: (1) no echocardiographic gold standard of RV functional assessment; (2) poor reproducibility; (3) two-dimensional echocardiographic measurements are obtained in a four-chamber view, which is only a single view. MPS has been widely used in coronary heart disease and HF. If the indicators measuring RV function in MPS were discovered, it will benefit a large number of patients by reducing the patient examinations and saving medical resources.

#### **5. Conclusion**

We proposed a spatial temporal V-Net to automatically extract RV epicardial and endocardial contours from gated MPS. The proposed S-T-V-Net fully used the spatial features from the three-dimensional gated MPS by V-Net, and the temporal correlations from the MPS sequential imaging using ConvLSTM. It was validated on our dataset with 34 subjects and produced accurate results for both RV segmentation and RVEF measurement. The proposed deep learning model would provide auxiliary supports in clinical practice for RV functional assessment in MPS.

## Reference

- [1] J. Liu, L. Fei, G.-Q. Huang, X.-K. Shang, M. Liu, Z.-J. Pei, Y.-X. Zhang, Right ventricle performances with echocardiography and 99mTc myocardial perfusion imaging in pulmonary arterial hypertension patients, *Experimental Biology and Medicine*, 243 (2018) 754-761.
- [2] L. Wang, X. Ma, L. Xiang, M. Lu, C. Yan, S. Zhao, W. Fang, The characterization and prognostic significance of right ventricular glucose metabolism in non-ischemic dilated cardiomyopathy, *Journal of Nuclear Cardiology*, 23 (2016) 758-767.
- [3] L. Wang, X. Shang, M. Xiaoli Lan, Semi-quantitative assessment of pulmonary arterial hypertension associated with congenital heart disease through myocardial perfusion imaging, *Hellenic journal of nuclear medicine*, 20 (2017) 204-210.
- [4] G. Germano, P.B. Kavanagh, P. Waechter, J. Areeda, A new algorithm for the quantitation of myocardial perfusion SPECT. I: technical principles and reproducibility, *The Journal of Nuclear Medicine*, 41 (2000) 712.
- [5] C. Huang, X. Shan, Y. Lan, L. Liu, H. Cai, W. Che, Y. Hao, Y. Cheng, Y. Peng, A hybrid active contour segmentation method for myocardial D-SPECT images, *IEEE Access*, 6 (2018) 39334-39343.
- [6] H. Sonesson, J.F. Ubachs, M. Ugander, H. Arheden, E. Heiberg, An improved method for automatic segmentation of the left ventricle in myocardial perfusion SPECT, *Journal of Nuclear Medicine*, 50 (2009) 205-213.
- [7] J. Betancur, M. Rubeaux, T.A. Fuchs, Y. Otaki, Y. Arnson, L. Slipczuk, D.C. Benz, G. Germano, D. Dey, C.-J. Lin, Automatic valve plane localization in myocardial perfusion SPECT/CT by machine learning: Anatomic and clinical validation, *Journal of Nuclear Medicine*, 58 (2017) 961-967.
- [8] T. Wang, Y. Lei, H. Tang, J. Harms, C. Wang, T. Liu, W.J. Curran, W. Zhou, D. Li, X. Yang, A learning-based automatic segmentation method on left ventricle in SPECT imaging, *Medical Imaging 2019: Biomedical Applications in Molecular, Structural, and Functional Imaging*, International Society for Optics and Photonics 2019, pp. 109531M.
- [9] F. Haddad, S.A. Hunt, D.N. Rosenthal, D.J. Murphy, Right ventricular function in cardiovascular disease, part I: anatomy, physiology, aging, and functional assessment of the right ventricle, *Circulation*, 117 (2008) 1436-1448.
- [10] A. Van Tosh, K.J. Nichols, *Ventricular asynchrony: A shift to the right?*, Springer 2017.
- [11] L. Wang, W. Zhou, Y. Liang, Y. Yang, E.V. Garcia, J. Chen, W. Fang, Right ventricular dyssynchrony in pulmonary hypertension: Phase analysis using FDG-PET imaging, *Journal of Nuclear Cardiology*, 24 (2017) 69-78.
- [12] W. Zhou, Z. Jiang, J. Chen, E.V. Garcia, D. Li, Development and validation of a phase analysis tool to measure interventricular mechanical dyssynchrony from gated SPECT MPI, *Journal of Nuclear Cardiology*, 24 (2017) 1680-1686.
- [13] F. Milletari, N. Navab, S.-A. Ahmadi, V-net: Fully convolutional neural networks for volumetric medical image segmentation, 2016 fourth international conference on 3D vision (3DV), IEEE 2016, pp. 565-571.

- [14] S. Ioffe, C. Szegedy, Batch normalization: Accelerating deep network training by reducing internal covariate shift, *International conference on machine learning*, PMLR2015, pp. 448-456.
- [15] S. Hochreiter, J. Schmidhuber, Long short-term memory, *Neural computation*, 9 (1997) 1735-1780.
- [16] S. Xingjian, Z. Chen, H. Wang, D.-Y. Yeung, W.-K. Wong, W.-c. Woo, Convolutional LSTM network: A machine learning approach for precipitation nowcasting, *Advances in neural information processing systems*2015, pp. 802-810.
- [17] C.H. Sudre, W. Li, T. Vercauteren, S. Ourselin, M.J. Cardoso, Generalised dice overlap as a deep learning loss function for highly unbalanced segmentations, *Deep learning in medical image analysis and multimodal learning for clinical decision support*, Springer2017, pp. 240-248.
- [18] M.J. Cardoso, T. Arbel, G. Carneiro, T. Syeda-Mahmood, J.M.R. Tavares, M. Moradi, A. Bradley, H. Greenspan, J.P. Papa, A. Madabhushi, Deep learning in medical image analysis and multimodal learning for clinical decision support, (2017).
- [19] Y. Li, C. Fang, J. Yang, Z. Wang, X. Lu, M.-H. Yang, Flow-grounded spatial-temporal video prediction from still images, *Proceedings of the European Conference on Computer Vision (ECCV)*2018, pp. 600-615.
- [20] S. Ghio, A. Gavazzi, C. Campana, C. Inserra, C. Klersy, R. Sebastiani, E. Arbustini, F. Recusani, L. Tavazzi, Independent and additive prognostic value of right ventricular systolic function and pulmonary artery pressure in patients with chronic heart failure, *Journal of the American College of Cardiology*, 37 (2001) 183-188.
- [21] T.M. Gorter, E.S. Hoendermis, D.J. van Veldhuisen, A.A. Voors, C.S. Lam, B. Geelhoed, T.P. Willems, J.P. van Melle, Right ventricular dysfunction in heart failure with preserved ejection fraction: a systematic review and meta-analysis, *European journal of heart failure*, 18 (2016) 1472-1487.
- [22] R. Woog, D. McWilliam, A comparison of methods of cardiac output measurement, *Anaesthesia and intensive care*, 11 (1983) 141-146.